RESEARCH ARTICLE

Open Access

The design, fabrication, and structural and embodied carbon analysis of the world's first manufactured topologically optimised multi-metal I-beam



Efstathios Damtsas^{1*}, Alejandro Nieto Jiménez², Marina Konstantatou³, Michael Herrmann¹ and Kostas Grigoriadis⁴

Abstract

This research focuses on the design, fabrication, and structural and embodied carbon analysis of the world's first topologically optimised multi-metal I-beam. Specifically, the beam under study is a European Parallel I-beam with a nominal height of 100 mm (commonly referred to as 'IPE-100'), and the materials used are mild steel and tool steel. Topology Optimisation (TO) is performed using Altair's OptiStruct software package, applying the Solid Isotropic Material with Penalty (SIMP) method. The multi-metal beam is fabricated using 3D printing, specifically Laser Metal Deposition (LMD), with a dual built-in metal wire feeder attached to a robotic arm. The beam is analysed both environmentally and structurally — the former focusing on an embodied carbon assessment of material extraction and component manufacturing, and the latter on four-point structural load testing. The fabrication method and analysis results are compared with those of the standard IPE-100 beam currently used in construction. Environmentally, the Multi-Material Topologically Optimised (MMTO) beam's reduced mass results in lower carbon emissions compared with the standard IPE-100; however, due to the high emissions associated with its fabrication process, its overall carbon footprint is higher. Structurally, the MMTO beam can withstand a higher machine load than the standard IPE-100 before undergoing plastic deformation. This research is the result of an international, multidisciplinary collaboration between academia and industry across the United Kingdom, Germany, and Spain.

Keywords Multi-metal 3d printing, Multi-material topology optimisation, Laser metal deposition, Embodied carbon analysis, Four-point structural testing

*Correspondence: Ffstathios Damtsas

efstathios.damtsas@th-luebeck.de

1 Introduction

The research presented in this paper focuses on the topological optimisation (TO) and additive manufacturing (AM) of a structural building component—specifically, an I-beam. The primary objective is to reduce the beam's mass and, consequently, its embodied carbon. The test case involves an IPE-100 section, which is typically made from S235 steel and features a uniform I-profile along its length. The aim is to apply TO to utilise the beam as fully as possible under a given load, thereby reducing the amount of material required to perform the same



© The Author(s) 2025. **Open Access** This article is licensed under a Creative Commons Attribution 4.0 International License, which permits use, sharing, adaptation, distribution and reproduction in any medium or format, as long as you give appropriate credit to the original author(s) and the source, provide a link to the Creative Commons licence, and indicate if changes were made. The images or other third party material in this article are included in the article's Creative Commons licence, unless indicated otherwise in a credit line to the material. If material is not included in the article's Creative Commons licence and your intended use is not permitted by statutory regulation or exceeds the permitted use, you will need to obtain permission directly from the copyright holder. To view a copy of this licence, visit http://creativecommons.org/licenses/by/4.0/.

¹ Faculty of Architecture and Urban Planning and Faculty of Civil and Environmental Engineering, Bauhaus-University Weimar, Weimar, Germany

² Department of Product Development, Meltio, Jaen, Spain

³ Specialist Modelling Group, Foster and Partners, London, UK

⁴The Bartlett School of Architecture, Faculty of the Built Environment, University College London, London, UK

structural function as a standard beam, but in a more sustainable manner.

The TO of structural metal beams has been extensively researched (Amir & Mass, 2018; Chiu et al., 2018; Habashneh & Rad, 2024; Kingman et al., 2014; Lagaros et al., 2008; Laghi et al., 2022; Ribeiro et al., 2021; Robbins et al., 2016; Tsavdaridis et al., 2014, 2015; Ye et al., 2021), but such studies mainly focus on single material optimisation. The very few research projects on TO with multiple materials either investigate the combination of different polymers (Esfarjani et al., 2022) or of steel and concrete (Li & Xie, 2021; Wethyavivorn et al., 2022). The current research builds upon this work and, for the first time, investigates the use of two metals in the TO and AM of a building component. A general 500-word overview of this research project was included in 3D Printing and Material Extrusion in Architecture (Grigoriadis & Lee, 2024); however, this article presents a detailed, indepth analysis of a specific aspect of the work, focusing on design, fabrication, and analysis.

Meltio can 3D print with a range of metals, including mild steel ER70-S, stainless steel (316L, 308L, and 17-4PH), tool steel H11, invar, titanium, and nickel (718 and 625) (Meltio3D, 2025). The first hypothesis was that using a metal from this range with higher structural strength than S235 would result in a significantly lower component mass. Tool steel H11, which has approximately six times the yield strength and five times the tensile strength of S235 (Table 1), was therefore selected as the first material for the TO to be used in regions subject to higher loading. However, as discussed in Sect. 4, the production of raw tool steel results in carbon emissions of 2.287 kgCO₂e/kg, compared with 2.107 kgCO₂e/kg for S235. Given that S235 cannot currently be 3D printed, the second assumption was that introducing a secondary metal-with a lower carbon footprint than tool steel and structural properties similar to S235—would minimise the overall carbon footprint. Mild steel ER70-S was selected as this secondary material due to its comparable tensile strength and Young's modulus to S235 (Table 1), as well as its similar carbon emissions from raw material production (2.124 kgCO $_2$ e/kg). It was therefore designated for use in regions of the TO beam subject to lower loading. In summary, the approach assumed that a high-performance steel would achieve maximum mass reduction, while the inclusion of a lower embodied carbon steel would minimise the total carbon footprint.

Lastly, it should be noted that both metals are used here in unconventional ways: mild steel is generally used as a filler material in wire arc additive manufacturing (WAAM) (Zhai et al., 2024) rather than a structural component, and tool steel is used in dies (Persson et al., 2005). Furthermore, although tool steel offers higher strength and mild steel lower embodied carbon, neither is suitable for conventional I-beams. Tool steel requires specialised machining rather than standard hot rolling as it is prone to solidification cracking (Hashimoto et al., 2009). Higher carbon steels such as tool steel are also more expensive than low-carbon steels such as S235 (Met al. &Tek International, 2024), offering no economic advantage over regular-grade alternatives (Saufnay et al., 2021).

Effectively, excluding the potential higher cost, this study focuses on the design and fabrication of the TO dual-metal IPE-100 beam, together with a comparative analysis of its structural performance and embodied carbon relative to a standard full-mass equivalent. Section 2 details the TO design methodology. Section 3 outlines the AM process used to produce the dual-metal beam. Section 4 presents an embodied carbon assessment covering both material production and component fabrication, comparing the resulting CO₂ emissions with those of the standard beam. Section 5 provides detailed structural analyses of four beam variants: a standard IPE-100 beam; an IPE-100 beam 3D printed in mild steel; a single material TO (SMTO) IPE-100 beam 3D printed in mild steel; and a multi-material TO (MMTO) IPE-100 beam 3D printed using both mild and tool steel. The concluding section summarises the key findings and outlines the next steps for this research.

Table 1 Comparison of material and structural properties of various steel types

| Material | Yield Strength (MPa) | Tensile Strength (MPa) | Young's Modulus (MPa) | Poisson's Ratio | Density (kg/m³) |
|-------------------|-------------------------|---------------------------|-----------------------|-----------------|--------------------|
| Mild Steel ER70-S | 402±37 | 525±12 | 195,000–205,000 | 0.300 | 7,800 |
| Tool Steel H-11 | 1,482 | 1,792 | 210,000 | 0.285 | 7,800 |
| 308 LSI | 240 | 580 | 193,000 | 0.285 | 8,000 |
| S235 | 215–235 | 360 | 210,000 | 0.300 | 7,850 |

2 Designing the Multi-Material Topologically Optimised (MMTO) Beam

A one-metre-long standard IPE-100 beam was modelled as a closed extrusion in McNeel's Rhinoceros3D (Rhino), providing the starting geometry for the TO process. To carry out the optimisation, the Rhino model was exported as .STEP files and assembled in parts within a HyperMesh session of Altair HyperWorks 2022, using an OptiStruct profile.

The imported geometry was divided into "design" and "non-design" components: the design component could undergo material reduction during the TO, while the non-design component remained unchanged. The less stiff of the two materials (mild steel) was initially assigned to both components, while the placement of the stiffer material (tool steel H11) was determined by Altair's Opti-Struct algorithm, which uses the Solid Isotropic Material with Penalty (SIMP) method. The algorithm assigns a pseudo-material density (ρ) and determines whether an element will be solid $(\rho = 1)$ or void $(\rho = 0)$ using a power-law penalisation for the stiffness-density relationship (Altair Engineering Inc., 2021a). Both components were assigned a PSOLID property to match the imported geometry type, which was a three-dimensional solid. The units used in the design setup were newtons (N), millimetres (mm), and tonnes (T).

To generate the finite elements required for TO, the solid geometry was converted into a Tetramesh, which is "an enclosed volume with first or second order tetrahedral elements" (Altair Engineering Inc., 2021b). A minimum mesh element size of 10 mm, combined with the application of symmetry along the XZ plane, resulted in a fine mesh comprising 263,535 Tetramesh elements. The software offered limited control over the meshing process, which was carried out automatically using the Delaunay method to fill the design space. The input dimensions, along with the positions of the loads and supports, matched those used in the physical testing

presented in Sect. 5. Specifically, a total load of 1 kN was applied across 293 nodes within the designated regions on either side of the beam (Fig. 1a).

The supports were defined as Single Point Constraints (SPCs) and positioned on the non-design elements at either end of the beam, as illustrated in Fig. 1(b). This configuration allowed each support to rotate about the x-axis while preventing it from toppling along the y-axis. The complete optimisation setup is shown in Table 2.

The primary objective of the optimisation was to reduce the mass of the beam's design component while

Table 2 Optimisation setup parameters

| Category | Altair (PSOLID) | | |
|-----------------------|---|--|--|
| Mesh | TetraMesh (CTETRA4) | | |
| Average Mesh Size | 1.560 | | |
| Minimum Element Size | 10 | | |
| Number of Elements | 263,535 | | |
| Volume Fraction (%) | On 50% Overall Volume Fraction: • 30% mild steel (remaining) • 70% tool steel (upper bound) | | |
| Poisson's Ratio | • 0.300 (mild steel) • 0.285 (tool steel) | | |
| Young's Modulus (MPa) | 195,000 MPa (mild steel)210,000 MPa (tool steel) | | |
| Mass Density | $7.800e^{-09}$ (both mild steel and tool steel) | | |
| Elements supported | 2 parallel per side | | |
| Penal | 3 (1st phase) and 4 (2nd and 3rd phase) (Altair Engineering Inc., 2024, (Altair 2025b) | | |
| Number of Iterations | 48 (maximum allowed 80) | | |
| Load (N) | (0,0,-1000) (3,414 N on 293 nodes per side) | | |
| Material | mild Steel ER70-Stool Steel H-11 | | |
| Supports | Fixed: Ty,Tz,Rx (Left) Fixed: Tx,Ty,Tz,Rx (Right) | | |
| Convergence Tolerance | 0.005 | | |
| Step Size | 0.500 | | |
| TO Method | Density (SIMP) (Altair Engineering Inc., 2025a) | | |
| | | | |

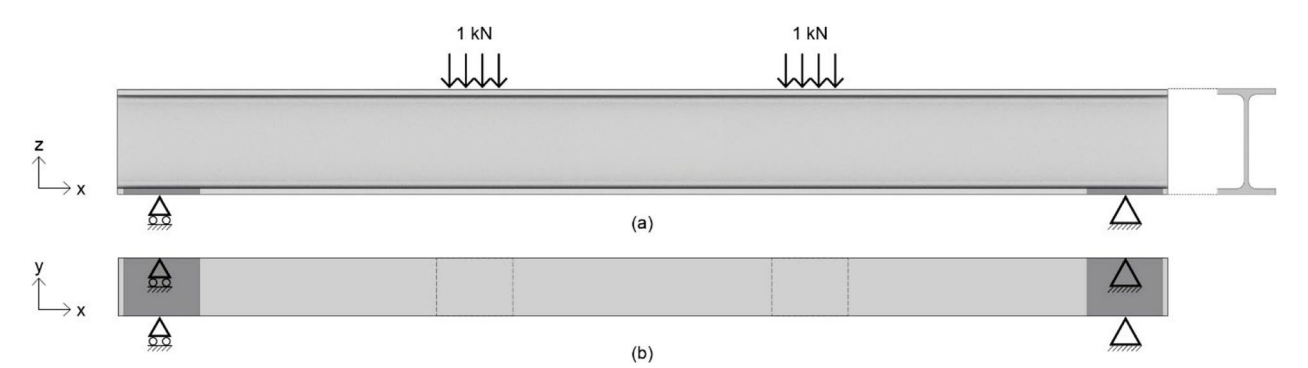


Fig. 1 Geometric setup for optimisation in Altair HyperWorks showing loads, support point constraints, the design region (light grey), non-design regions (dark grey) and axes: (a) front view; (b) bottom view

maximising its stiffness, thereby minimising compliance. The reduction in tool steel mass was controlled by a custom mass ratio constraint (DCONSTR) with an Upper boundary ranging from 0.0 (no tool steel) to 1.0 (only tool steel). The constraint employed a function response type (DRESP2) together with a design equation (DEQATN) card, the latter defining the functional relationship as f(a,b) = a/b. It combined two mass responses (DRESP1): the tool steel mass response and the minimise mass response (which minimised the total mass) (Altair Engineering Inc., 2022a; Hoglund, 2024). This constrained the proportion of tool steel permitted in the optimised design. In addition, the percentage of the beam's volume retained following optimisation was controlled using a volume constraint (DCONSTR), with an Upper boundary ranging from 0.1 (10% of the beam remaining) to 1.0 (100% of the beam remaining). This constraint employed a volume fraction response type (DRESP1) on the 'by entity' type PSOLID 'design' property. In OptiStruct, the volume fraction does not include the non-design volume and is calculated as shown in Eq. 1 (Altair Engineering Inc., 2022b). In summary, the beam's volume was first reduced according to the specified volume fraction, with the amount of tool steel further limited by the mass ratio function. The optimisation objective—to minimise compliance via linear static analysis-was also specified. The formulation of static compliance is shown in Eq. 2 (Altair Engineering Inc., 2022b). The multiple materials used during the optimisation process were defined in the design variable DTPL card, which used a topology configuration assigned to the PSOLID design property. Finally, the optimisation settings in HyperWorks were exported as a .FEM file and executed using the OptiStruct solver within Altair's Compute Console.

Table 3 Optimisation combinations of overall volume fraction and mass ratio

| Overall Volume Fraction (%) | Mass Ratio Mild Steel ER70S (%) | Mass Ratio Tool Steel H11 (%) | |
|-----------------------------|---------------------------------------|--|--|
| $\overline{\phi_i}$ | 0 | 100 | |
| φ_i | 10 | 90 | |
| φ_i | 20 | 80 | |
| Φ_i | 30 | 70 | |
| φ_i | 40 | 60 | |
| φ_i | 50 | 50 | |
| φ_i | 60 | 40 | |
| φ_i | 70 | 30 | |
| φ_i | 80 | 20 | |
| φ_i | 90 | 10 | |
| Φ_i | 100 | 0 | |

Volume Fraction $(\varphi_i) = 10i$, where i = 1, 2, ..., 10

that the 10% volume fraction did not yield meaningful results, as discontinuities in the material distribution rendered the optimised components structurally unviable (Fig. 2).

Furthermore, volume fractions corresponding to less than 50% mass reduction failed to remove sufficient material to achieve significant decreases in mass or embodied carbon (Shah et al., 2023).

Across most of the remaining volume fraction increments (i.e., from 20% to 50%), a 10%–90% mild steel (MS) to tool steel (TS) combination resulted in a TO design composed entirely of tool steel. Conversely, the 70%–30%, 80%–20%, and 90%–10% MS–TS combinations produced designs made entirely of mild steel—none of which were suitable for the purposes of this study. The

$$Volume\ fraction = \frac{((total\ volume\ at\ current\ iteration) - (initial\ non - design\ volume))}{initial\ design\ volume} \tag{1}$$

$$C = \frac{1}{2}u^T f \tag{2}$$

where C denotes compliance, u^T means the transpose of the displacement vector, and f is the applied force vector, which is a product of the stiffness matrix and the displacement vector (Altair Engineering Inc., 2022b).

The optimisation was performed for all volume fractions in 10% increments. Each volume fraction included all combinations of tool steel and mild steel, also in 10% increments. Table 3 provides a detailed overview of this setup. The aim was to gain a better understanding of the MMTO results and to identify the most suitable configuration for 3D printing. It became apparent

20%–80% (excluding the 20% volume fraction), 30%–70%, and 40%–60% (excluding the 40% volume fraction) MS–TS ratios yielded a distribution of tool steel concentrated in the structurally critical regions of the beam, aligning with the original objective of using a higher-performing steel in these areas. By contrast, mild steel dominated the key structural regions in the 50%–50% (Fig. 3), 60%–40%, and 70%–30% combinations, rendering these configurations unviable.

It was therefore evident that only the 20%–80%, 30%–70%, and 40%–60% MS–TS combinations produced viable results across all volume fraction increments. However, as previously noted, the 10% and 60%–90%

volume fractions were unusable. In the remaining 20% to 40% volume fractions, the usable MS-TS combinations featured steep members that required extensive support structures, increasing design and fabrication time, as well as embodied carbon. At the 50% volume fraction, the 40%-60% beam placed mild steel in part of the top region undergoing the greatest displacement, while the 20%-80% beam contained less MS than the 30%-70%

beam and therefore would exhibit higher embodied carbon. Accordingly, within these constraints, the 50% volume fraction with a 30%–70% mild steel—tool steel ratio (Fig. 4) was selected for printing, as it demonstrated a distribution of tool steel consistent with the displacement analysis and required less complex support structures, making it feasible within the research project's time-frame. All optimisation results are presented in Fig. 5.

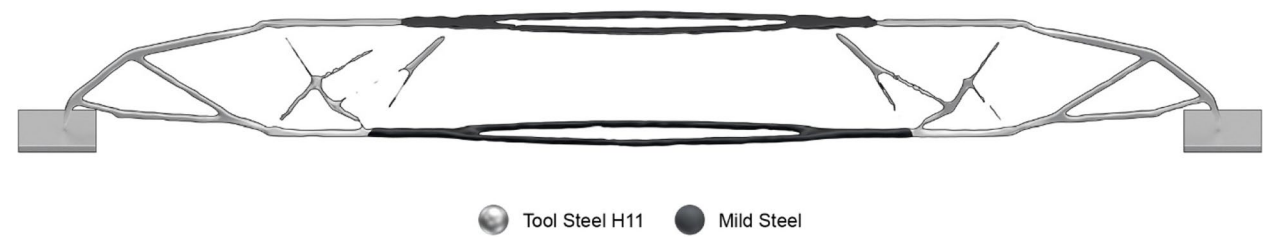


Fig. 2 The 10% volume fraction MMTO beam with a 60% mild steel and 40% tool steel distribution, showing the discontinuities in material distribution

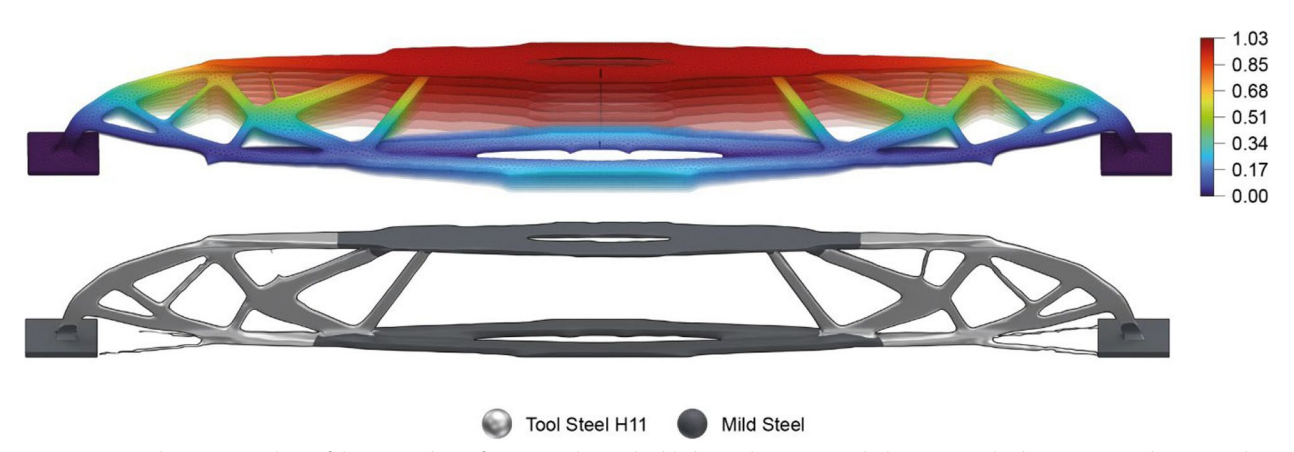


Fig. 3 Top: Displacement analysis of the 30% volume fraction TO beam, highlighting the region with the greatest displacement in red. Bottom: The MMTO beam with a 50% mild steel and 50% tool steel distribution, showing mild steel occupying the structurally critical red region—which should be filled with the higher-performing tool steel

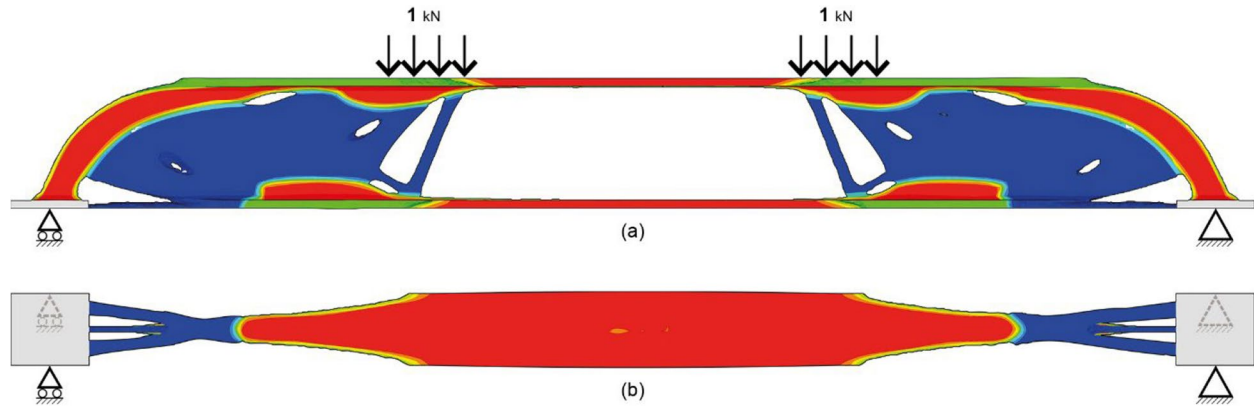


Fig. 4 Optimised result (50% volume fraction and 30%—70% Mild Steel – Tool Steel): (a) front view (b) bottom view

Damtsas et al. Architectural Intelligence

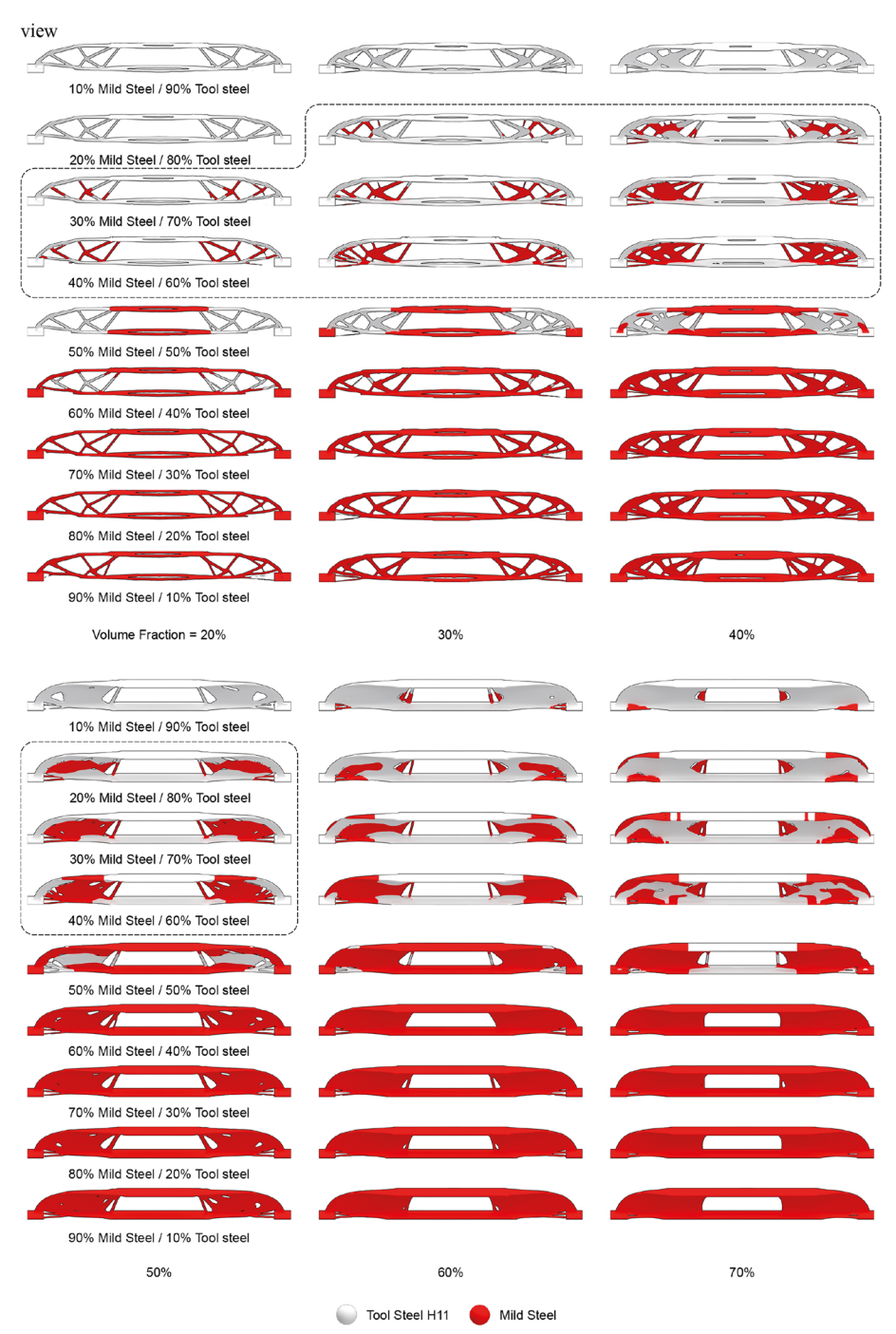


Fig. 5 Optimisations for volume fractions ranging from 20% to 70%, with mass ratios increasing in 10% increments. The results enclosed within the dashed-line frames represent the usable outputs

Once the optimisation converged to a feasible design, the *_des.h3d output file was imported into Altair's HyperView for visualisation and export. A contour plot showing the element densities of the components was generated, and the iso values of the TO results were displayed. This data was then exported from HyperView in .

stl format and imported into Rhino for post-processing in preparation for AM. To ensure continuity between the two materials—without averaging at their interface—the entire geometry was exported as a single density model and smoothed in Rhino using the Grasshopper plugin Weaverbird. The same process was then repeated for

each material individually, generating separate .stl files. Following smoothing, the mesh outline of either the tool steel or mild steel—depending on which was continuous and less geometrically complex—was extracted, extruded, and used to separate the two materials from the smoothed density model (Fig. 6).

A limitation of this method was that cutting could only be performed along a single two-dimensional plane. As a result, any "nested" material located in the perpendicular plane—as illustrated in Fig. 7—was excluded. Consequently, the design selected for fabrication and comparison with the standard IPE-100 beam did not include the nested material region. That said, the volume of these nested regions was negligible, and therefore their omission did not affect the structural performance

or carbon footprint of the overall beam. In future studies, should this volume prove considerable, the nested regions could be copied across from step (c) in Fig. 6 to step (g) using a common fixed reference point, and "Booleaned out" of the final geometry. Finally, as the optimisation result was slightly asymmetrical, the optimised beam was split at the midpoint and mirrored, preserving the side with the slightly lower mass.

3 Fabricating the Multi-Material Topologically Optimised (MMTO) Beam

This section discusses the fabrication of the MMTO beam, focusing on geometry importation, the fabrication method, and the associated limitations. It also outlines strategies used to mitigate these limitations, including the

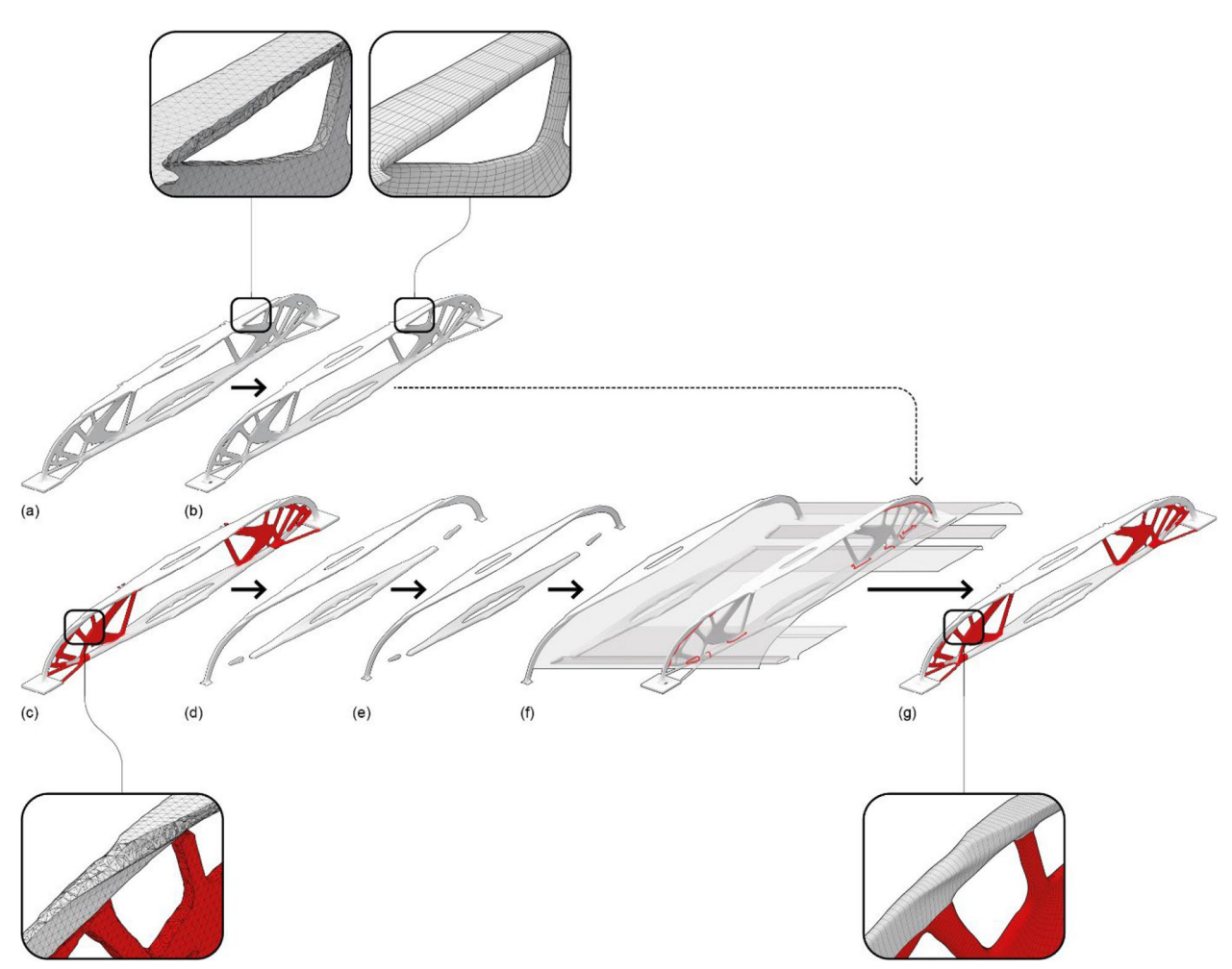


Fig. 6 Diagram of the mesh smoothing process: (**a**) Initial unprocessed, full density mesh exported from Optistruct and used as a single-material geometry for the splitting process; (**b**) Full density mesh (**a**) smoothed using Weaverbird for Grasshopper; (**c**) Unprocessed, dual-material mesh exported individually from Optistruct; (**d**) Tool steel segment of the dual-material mesh (**c**) before smoothing; (**e**) Tool steel smoothed using Weaverbird for Grasshopper; (**f**) Smoothed tool steel mesh outline extracted, extruded, and used to split the smoothed single-material density mesh (**b**); (**g**) Final smoothed, dual-material mesh

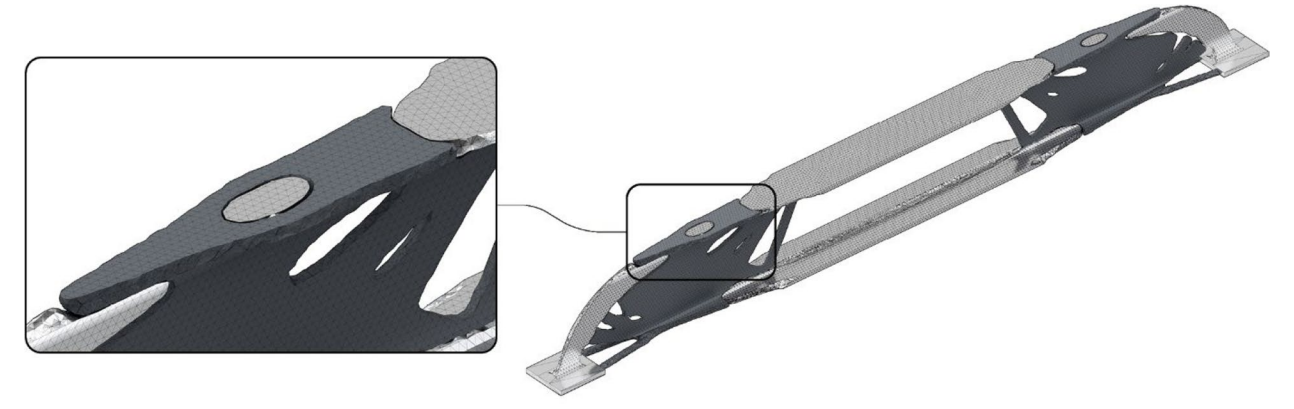


Fig. 7 Nested material in the perpendicular plane

implementation of intelligent supports and drop-shaped holes. In addition, it describes the pre- and post-fabrication processes—such as support removal and sandblasting of the beam—undertaken to ensure that the printed beam accurately reflects the digital TO geometry and clearly distinguishes between the two printed materials.

3.1 Chosen fabrication method and rationale

Meltio's multi-laser and dual-wire technology was used to fabricate the MMTO beam, as it allows for precise and efficient control over the fusion of two metals. Continuous, layer-by-layer deposition was achieved through the integration of two mechanisms: an advanced infrared laser configuration and a wire-fed Laser Metal Deposition (LMD) system.

The first mechanism consisted of six 976 nm direct diode lasers with a combined power output of 1,200 W. Used in conjunction with fibre optics and collimators, these lasers provided a highly focused energy source capable of efficiently and consistently melting the feed-stock wires, ensuring optimal bonding between layers and materials. The second mechanism involved two independent wire feeders, which supplied off-the-shelf mild steel and tool steel wire to a single deposition head mounted on an industrial robotic arm (Fig. 8). This setup enabled seamless transitions between the two metals, allowing for precise material deposition as required. The predictability and stability of the process eliminated the need for continuous monitoring or mid-print adjustments, resulting in a single, uninterrupted print.

3.2 Limitations of the fabrication method and mitigations

While the Meltio system offers several advantages, it also presents certain limitations when depositing material on overhangs—particularly in complex geometries such as those produced through TO. Depending on the slicing plane, the system can accommodate overhangs

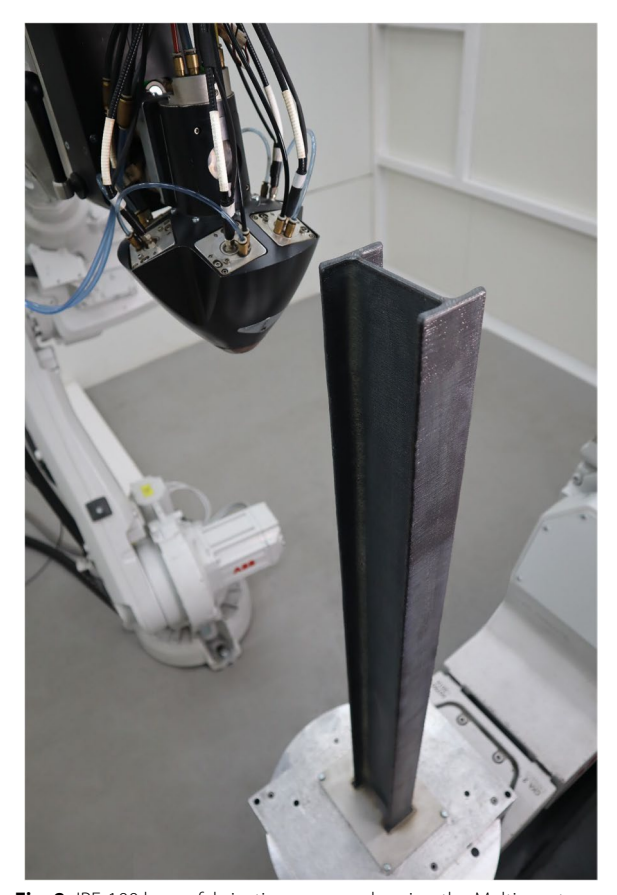


Fig. 8 IPE-100 beam fabrication process showing the Meltio system setup (photo by Meltio)

of up to 20 to 25 degrees from the vertical axis without requiring additional support structures. However, the elongated form and internal voids of the MMTO beam occasionally produced overhangs exceeding this threshold. To address this issue, as discussed in Sect. 3.3, intelligent support strategies were employed to identify

and reinforce critical areas. In future studies, this issue could be resolved by employing an overhang angle constraint in the DTPL card of Altair's setup. This could either entirely limit the overhangs to the desired angle using the Constraint method or minimise them using the softer Penalty method. The latter would allow some overhangs to exceed the specified angle to achieve a more optimised overall geometry but would also result in certain overhangs requiring supports (Hoglund & Fuerle, 2018). Figure 9 presents preliminary results of constraining the overhang to 25 degrees from the printing axis in a single material TO example.

An alternative approach that was considered involved non-planar or angled planar slicing, allowing the beam to be printed in multiple orientations. This technique enables the printhead to move perpendicularly to the deposition plane, thereby avoiding overhangs altogether. It involves slicing the beam along non-horizontal or inclined planes that follow the part's topology (Fig. 10a). While this method could reduce or eliminate the need for support structures, it also presents several challenges. The most significant concern is the increased risk of collisions between the deposition head and previously printed sections, which could disrupt the printing process. In addition, variations in heating and cooling

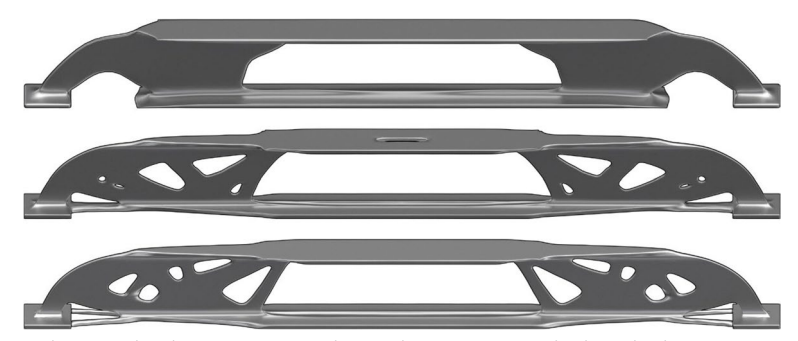


Fig. 9 From top to bottom, single material TO beams: constrained using the Constraint method (total volume: 0.00064 m³); constrained using the Penalty Method (total volume: 0.00055 m³); with no overhang angle constraint (total volume: 0.00055 m³)

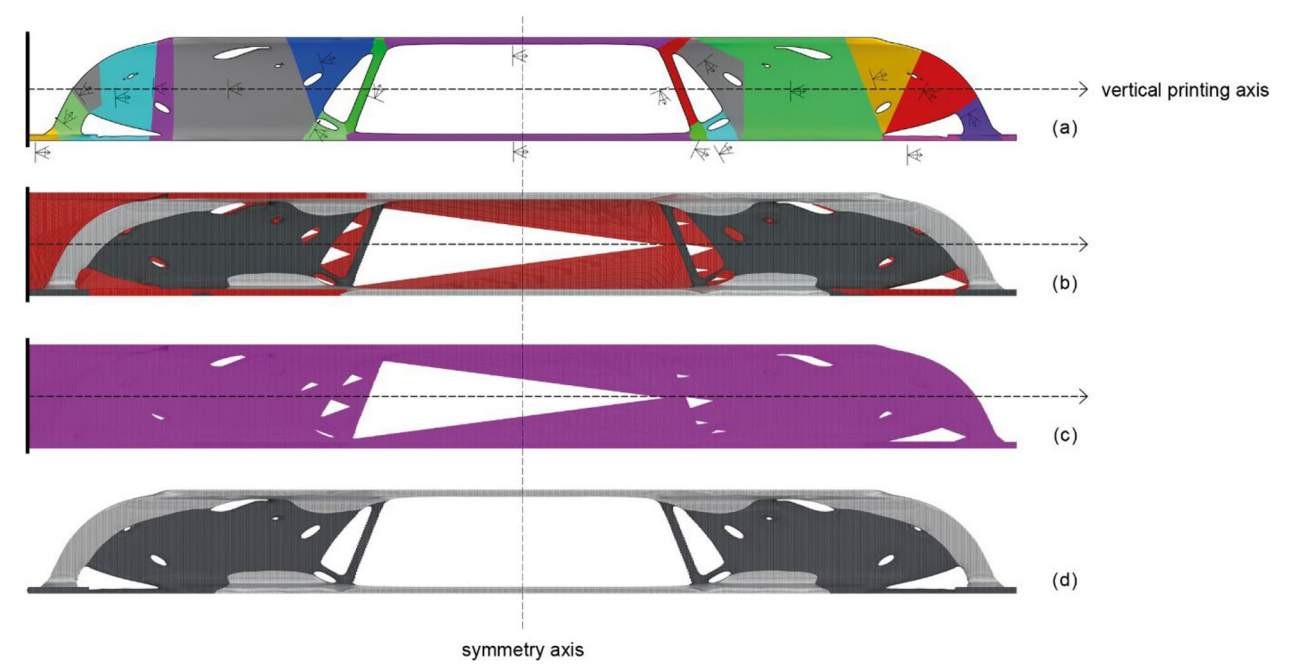


Fig. 10 Toolpath studies: (a) 50% volume fraction (30% mild steel and 70% tool steel) MMTO beam without supports—the different colours represent various printing orientations; (b) 50% volume fraction with 30% mild steel (black) 70% tool steel (grey) and supports (red) ensuring all overhangs are below 25 degrees from the vertical 3D printing axis; (c) final horizontal layer toolpath; (d) final printed beam without supports

across differently oriented layers may induce differential stresses, potentially resulting in inconsistencies in structural performance. For these reasons, a standard three-axis slicing method was selected. Although this approach necessitates the use of support structures (Fig. 10b), it provided a more stable and predictable fabrication process for the purposes of this study.

3.3 Pre-construction, construction and post-construction process

3.3.1 Pre-construction process

The first step in fabricating the MMTO beam involved importing the TO geometry into Rhino for post-processing. The mesh was carefully inspected for errors, which often requires manual correction. It was essential to ensure that the geometry was continuous, with no gaps or overlaps between the meshes of the two materials. Gaps can cause toolpath calculation errors and result in poor print quality, while overlaps may introduce voids, leading to structural defects. A smooth, error-free mesh is critical for ensuring consistency and structural integrity during manufacturing. The mesh was then organised into two separate layers—one for each material—which allowed for better control during the printing process and ensured precise material deposition.

The TO geometry was further refined to minimise overhang-related issues. As the Meltio Space software did not support automated drop-shaped supports at the time of fabrication, these structures had to be manually designed. They were created within the allowable overhang limits for each void, without altering the geometry of the TO beam itself. The drop-shaped design of the supports was specifically intended to minimise material usage and reduce printing time, while maintaining the structural integrity of the part during fabrication.

Meltio's software also played a key role in managing printing parameters. The wire feeders were programmed to account for the material-specific properties of mild steel and tool steel, ensuring that each was deposited using the appropriate energy density. Additionally, the slicer generated a toolpath with 100% solid infill to ensure that the printed beam matched Altair's optimised result.

3.3.2 Construction process

After the code was generated in the specific robot language, ABB Rapid, the robot program communicated with the Meltio Engine through Digital Inputs and Outputs, triggering various procedures such as starting the lasers and wire feeding process in synchronisation with the robot's movements. The beam's fabrication strategy involved two perimeter passes and continuous zigzag infill, with the infill direction rotating 45 degrees (Fig. 11)

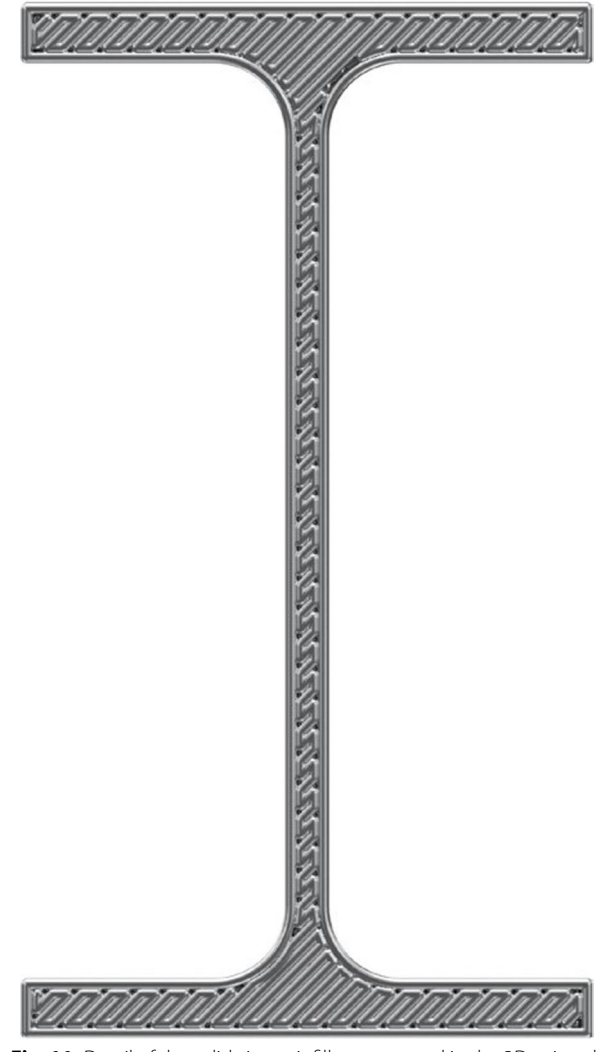


Fig. 11 Detail of the solid zigzag infill pattern used in the 3D-printed IPE-100 beam

with each layer to homogenise heat distribution throughout the process. The additive process was carried out in a closed environment, protecting technicians from laser radiation and ensuring safety from potential robot collisions, all controlled by a dual-channel safety circuit.

3.3.3 Post-construction process

After the MMTO beam was printed, it underwent post-processing (Fig. 12). This included the removal of support structures using Wire EDM technology— a non-traditional machining process that offers high precision (Fig. 13). Alternatively, band saw cutting could be used for this purpose, although it provides less precision. In addition, the beams were sandblasted to highlight the distinction between the two materials for aesthetic purposes, without affecting the structural performance of the component (Fig. 14).



Fig. 12 The MMTO (top) and SMTO (bottom) 3D printed beams before support removal and sandblasting (photo by Meltio)



Fig. 13 Detail of the wire EDM-cut support location (photo by Aaron Hargreaves/Foster+Partners)



Fig. 14 The 3D printed MMTO beam following support removal and sandblasting (photo by Aaron Hargreaves/Foster+Partners)

Finally, some sections of the beam also required further smoothing or residual stress-relief treatments to minimise the risk of internal stresses or deformations resulting from the AM process. These steps were essential to ensure the beam's performance under operational conditions. However, depending on the specific

application, further adjustments or refinements—such as optimising feed rate and cutting speed (Jayasankar et al., 2024) —may be necessary.

3.4 Printing parameters and material quantities for IPE-100 beams

In total, three beams were printed (Fig. 15) to evaluate the effectiveness of the TO and MMTO approach. Table 4 shows the printing parameters and material quantities for each beam.

Using Meltio's method, the MMTO beam took 67 h and 21 min to print. In contrast, standard IPE-100 beams produced using conventional methods such as rolling can be manufactured much more rapidly (Stahlwerk Thuringen GmbH, 2025). However, while the LMD process is slower, it enables the creation of complex geometries that are unachievable using traditional manufacturing techniques. Furthermore, the current Meltio system—updated in November 2024—features a 1,400W blue laser, which can achieve deposition rates up to 2.5 times higher than those of the 1,200W infrared laser used in this project. The improvement in deposition efficiency depends on the material's ability to absorb the laser's wavelength. The blue laser offers better energy absorption across most metals and therefore results in enhanced deposition performance.

Furthermore, the use of TO ensured that material was strategically placed for optimal structural performance. In contrast, standard IPE-100 beams are designed for general structural loading conditions and lack the customisation enabled by AM. While mass-produced building components are reliable, AM allows for more bespoke parts, generated through TO, to meet specialised load-bearing requirements. As a result, the total amount of material used in the multi-material beam was 5.02 kg (excluding supports), compared to 7.85 kg of S235 (EurocodeApplied, 2025) used in a standard one-metrelong IPE-100 beam.

In conclusion, the above demonstrates the advantages of AM in applications requiring bespoke geometries and tailored material distribution. Although Meltio's

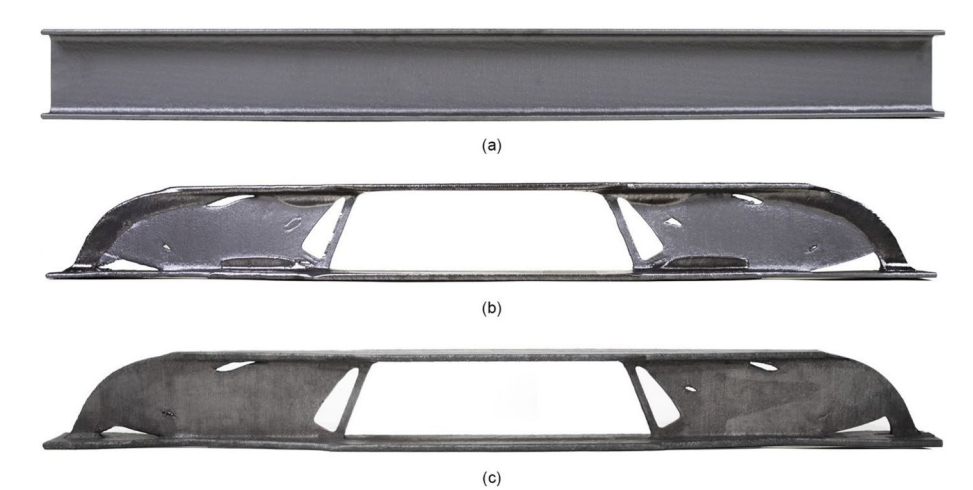


Fig. 15 Three of the 3D printed beams: (a) mild steel IPE-100 (b) mild steel – tool steel MMTO (c) mild steel SMTO for comparable structural comparison (photos by Meltio)

Table 4 LMD printing parameters used for fabricating the three beam types

| Print Parameters | IPE-100 beam (mild steel ER70S) | MMTO beam (mild steel ER70S + tool steel H11) | SMTO beam (mild steel ER70S) | |
|-----------------------------|------------------------------------|--|---------------------------------|--|
| Robot Speed (mm/s) | 7.500 | 6.500 | 6.500 | |
| Laser Power (W) | 1,100 | 830 (mild steel) 830 (tool steel) | 830 | |
| Feeder Speed (mm/s) | 7.570 | 8.280 | 8.280 | |
| Argon Flow (L/m) | 10 | 10 | 10 | |
| Printing Time (hrs:mins) | 29:37 | 67:21 | 67:21 | |
| Energy Density (J/mm³) | 185.010 | 127.630 (mild steel) 127.630 (tool steel) | 127.630 | |
| Deposition Rate (Kg/h) | 0.165 | 0.143 (mild steel) 0.143 (tool steel) | 0.143 | |
| Material Quantities | | | | |
| aterial 7.762 (g) | | 1.627 (mild steel) 3.394 (tool steel) | 4.584 | |
| Supports (Kg) | 0 | 2.194 | 2.049 | |
| Total (Kg) | 7.762 | 7.215 | 6.632 | |

method involves longer print times, its capacity to optimise dual material distribution within a single, automated process, while offering significant design flexibility, opens new opportunities in architecture and structural engineering. For certain applications—particularly those where performance optimisation is critical—MMTO components may offer a superior solution. Ultimately, the choice between traditional and AM methods will depend on the specific project

requirements, with AM presenting clear benefits for customised, high-performance applications.

4 Embodied Carbon Assessment of the Multi-Material Topologically Optimised (MMTO) Beam

As previously mentioned, the primary benefit of using TO and AM in building components is the reduction in mass, which is expected to lead to a corresponding decrease in embodied carbon. However, 3D printing

is an energy-intensive process, and the carbon savings achieved through mass reduction may be offset by the high energy consumption associated with manufacturing. Accordingly, this section presents an embodied carbon analysis comparing the standard IPE-100 with the MMTO beam to assess whether TO and AM indeed result in lower overall emissions.

4.1 Embodied carbon analyses (material production, rolling mill fabrication, casting, wire drawing and 3D printing) results

The embodied carbon assessment was completed according to the international standards BS EN ISO 14067:2018 Greenhouse Gases – Carbon Footprint of Products – Requirements and Guidelines for Quantification, Part 6: Methodology for Quantification of the CFP and Partial CFP; following a manner consistent with International Standards on Life Cycle Analysis (LCA) (ISO 14040 and ISO 14044) and The Greenhouse Gas Protocol. It addresses emission sources related to the production of steel materials and manufacturing. Material transportation activities were assumed to be insignificant and were not considered.

Based on a composition by weight of 97.3% Fe, 0.17% C, 1.4% Mn, 0.55% P, 0.03% S, and 0.55% Cu, the material production emissions for S235 steel were calculated at 2.107 kgCO₂e/kg. Assuming a rolling mill fabrication process, the emissions for manufacturing the I-beam were calculated at 0.264 kgCO₂e/kg. The volume of a 1 m IPE-100 beam is 0.001 m³. Therefore, the carbon emissions for material production and I-beam fabrication total 18.61 kgCO₂e (0.001m³ [S235 volume] ×7,850 kg/m³ [S235 density] × 2.371 kgCO₂e/kg [S235 material production and rolling mill fabrication]).

For the MMTO beam, based on a composition by weight of 97.6% Fe, 0.07% C, 1.45% Mn, 0.01% P, 0.02% S, and 0.85% Si for the mild steel, and 89.9% Fe, 0.35% C, 0.4% Mn, 1.1% Si, 5.5% Cr, 1.2% Mo, 0.25% V, and 1.3% W for the tool steel, the material production emissions were calculated as 2.124 kgCO₂e/kg and 2.287 kgCO₂e/kg, respectively. The slightly higher emissions for the tool steel are primarily due to the presence of chromium (Cr), whose extraction and processing are resource intensive. Casting and wire drawing—the processes used to produce the 3D printing feedstock for LMD—have carbon impacts of 0.495 kgCO₂e/kg and 0.068 kgCO₂e/kg, respectively.

The total volume of the MMTO beam is 0.00056m³, of which 0.000097m³ is mild steel and the remaining, tool

steel. This means that the carbon emissions for material and filament production are 2.05 kgCO₂e (0.000097m³ [mild steel volume] \times 7,850 kg/m³ [mild steel density] \times 2.69 kgCO₂e/kg [mild steel production, casting and wire drawing]) for the mild steel and 10.36 kgCO₂e (0.00046m³ [tool steel volume] \times 7,900 kg/m³ [average tool steel density] \times 2.85 kgCO₂e/kg [tool steel production, casting and wire drawing]) for the tool steel. This is a total of 12.41 kgCO₂e, which is lower than the standard beam, but without considering the 3D printing emissions.

Regarding the MMTO beam fabrication, as noted in Sect. 3.4, the total print time was 67 h and 21 min. According to Meltio, the energy consumption of the robot cell during the beam fabrication process was 4.5 kW per hour. Therefore, the total electricity consumption was 67.35 h×4.5 kW ≈303.08 kWh. Meltio's 4.5 kW energy figure includes all electricity-consuming processes within the robot system, as well as the chiller, and associated equipment consumptions. Using the "DEFRA (UK's Department for Environment Food and Rural Affairs) 2022 figure of 0.193 kgCO₂e per kWh unit" (Grigoriadis et al., 2024) the total equates to approximately 58.49 kgCO2e. This significantly increases the MMTO emissions, and this calculation does not yet account for the emissions from the use of argon gas in the process, which, according to Shah et al. (2023), increases the carbon footprint by "0.114 kg of CO₂ per kilogram of printed material." A summary of this section can be seen in Table 5 below.

4.2 Comparison of results with standard IPE-100/ discussion

It should be noted that, excluding the carbon footprint associated with standard I-beam rolling mill fabrication, its material production emissions amount to 16.5 kgCO₂e. This corresponds to an MMTO-to-standard beam volume ratio of 0.56, while the material production carbon emissions ratio is slightly higher, at approximately 0.75. These two figures differ because mild steel has a marginally higher embodied carbon than \$235, whereas tool steel has a substantially higher embodied carbon. Nevertheless, it is clear that volume reduction through TO also leads to a reduction in carbon emissions. However, the low deposition rate of 0.143 kg/h during 3D printing results in a very long fabrication time, which in turn contributes to significant additional carbon emissions.

Looking ahead, and as will be discussed in the conclusion, there are three key parameters to consider. First, increasing the deposition rate could substantially reduce the climate change impact. Second, the DEFRA emissions factor of 0.193 kgCO $_2$ e per kWh is expected to decline as the UK progresses towards its Net Zero 2050

¹ Emission factors for the constituent metals were taken from peerreviewed, previously published data sources.

Table 5 Embodied carbon analysis results for the standard IPE-100 and MMTO beam emissions. The Total Material + Filament Production Emissions figure excludes the supports, which weighed 2.19 kg and would have added 4.64 kgCO₂e

| Category | IPE-100 beam (S235) | MMTO beam (mild + tool steel) | |
|--|--|---|---|
| Composition by weight (%) | 97.3 (Fe) 0.17 (C) 1.4 (Mn) 0.55 (P) 0.03 (S) 0.55 (Cu) | mild steel: 97.6 (Fe) 0.07 (C) 1.45 (Mn) 0.01 (P) 0.02 (S) 0.85 (Si) | tool steel: 89.9 (Fe) 0.35 (C) 0.4 (Mn) 1.1 (Si) 5.5 (Cr) 1.2 (Mo) 0.25 (V) 1.3 (W) |
| Material Density (kg/m³) | 7,850 | mild steel: 7,850 | tool steel: 7,900 |
| Material Production Emissions (kgCO ₂ e/kg) | 2.107 | mild steel: 2.124 | tool steel: 2.287 |
| Beam Volume (m³) | 0.001 | mild steel: 0,000097 | tool steel: 0.00046 |
| | | total: 0.00056 | |
| Beam Fabrication Process | rolling mill | 3D printing | |
| Rolling Mill Fabrication Emissions (kgCO ₂ e/kg) | 0.264 | N/A | |
| 3D Printing Filament Production Emissions (kgCO $_2$ e/kg) | N/A | 0.495 (casting) 0.068 (wire drawing) | |
| Total Material Production + Beam Fabrication Emissions (kgCO ₂ e) | 18.61 | N/A | |
| Total Material + Filament Production Emissions (kgCO $_2$ e) | N/A | mild steel: 2.05 | tool steel: 10.36 |
| | | total: 12.41 | |
| Total Electricity Consumption Emissions for 3D Printing (kgCO $_{\!2}\!e)$ | N/A | (3D printing time: 67.35 h energy consumption: 4.5 kW total electricity used: 303.08 kWh emission factor: 0.193 kgCO₂e/kWh) total: 58.49 | |
| Additional Emissions (not included in the calculation) | N/A | argon gas: 0.114 kgCO ₂ /kg printed material | |

target. Third, the MMTO beam selected for fabrication had half the mass of the standard IPE-100; to achieve further reductions, beams with 60% or 70% lower mass will be investigated in the next phase of this research.

5 Structural Testing of the Multi-Material Topologically Optimised (MMTO) Beam

5.1 Specimens and test setup

The question that this section aimed to answer was whether the printed and optimised beams had an adequate structural performance compared to the rolled IPE-100 beam.

To investigate this, a series of structural tests were performed on a Zwick Universal testing machine at the MPA Schleswig Holstein facilities of TH Luebeck in Germany. A four-point bending test setup was chosen to determine the beams' load deflection curves. The main points of interest are the test load associated with the plastic yielding moment of the cross section, the transition from

elastic to plastic bending, bending stiffness, and the specimen's failure mode.

The rolled IPE-100 beam in Steel S235 has a plastic yielding moment $M_{y,pl,Rd}=9.3kNm$ with $y_{m0}=1.0$ and $f_y=235N/mm^2$ (Albert, 2024). From this yielding moment, a test load at yielding $F_{y,test}$ can be back-calculated from the bending moment distribution of a four-point bending test as $F_{y,test}/2=M_{y,pl,Rd}/0.3m$. Therefore $F_{y,test,100,235}=62kN$. This formula can be adapted for other material properties, e.g., for mild steel, where the correction factor is $f_{y,mildsteel}/235=402/235=1.71$.

Overall, four specimens (the three seen in Fig. 15 named in this section as B2, B1 and B3 respectively and a rolled S235 IPE-100 beam named B4) were weighed and then structurally tested vertically in two load steps in a four-point bending test (Fig. 16). The loading speed was determined in a pre-test on specimen B1 in such a way that a loading increment of 5 KN is reached within 300 s. This leads to a displacement speed of 0.02 mm/s

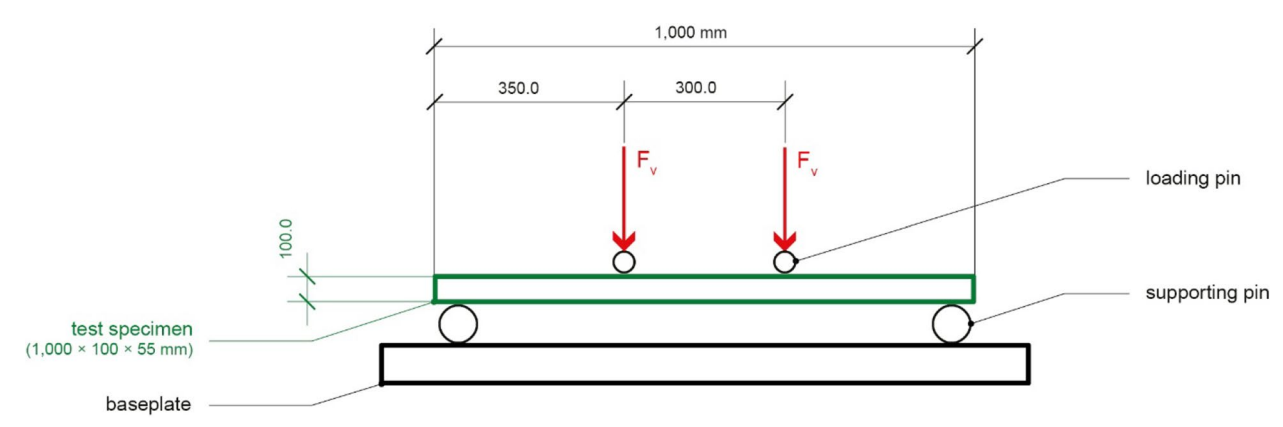


Fig. 16 Structural testing setup diagram

in the main test. In a first loading step the beams were loaded up to $F_{y,test,100,235} = 62kN$. After pausing, the test continued until failure loading up to F_{ultimate} .

Deflection was measured using the Machine Way (mm). The bottom beam of the testing machine (shown red in Fig. 17) is fully supported and thus assumed to be rigid. The upper loading beam (shown white in Fig. 17) is assumed to be within direct load transfer 1:2.5 and its deformations can be neglected. Therefore, the Machine Way is assumed to be close to the deflection of the test beam at the position of the upper load transfer points.

5.2 Results of testing (Multi-Material Topologically Optimised (MMTO) beam versus standard IPE-100)

Figure 18 shows the beam components after unloading, with some visible plastic deformation. While the optimised beams failed due to local buckling of the upper flange, the full beams failed due to lateral torsional buckling.

Figure 19 shows the load displacement diagram of all four beams. The horizontal dotted line is the test load $F_{y,test,100,235} = 62kN$ associated to $M_{y,pl,Rd}$ of B4. The three marked and highlighted boxes show isolated areas of interest of the tests (Fig. 20). All four beams pass $F_{y,test,100,235}$ without showing a loss of stiffness and therefore staying linearly elastic. Box 1 shows a shift in the load displacement curves within a range of approximately 1 mm, which can be explained by the initial contact and load transfer of all supports and load applications. After an initiation load of 2 kN all four curves develop almost parallelly showing similar elastic bending stiffnesses.

B3 was the first beam to reach its ultimate test load at approximately 75.7 kN with an initial decrease in stiffness around 70 kN. From this point, a local buckling behaviour of the upper flange can be observed with a decline in measured applied load. Component B4 reached its ultimate test load at 86 KN and its stiffness started to decrease at a loading level of approximately 80 kN. The

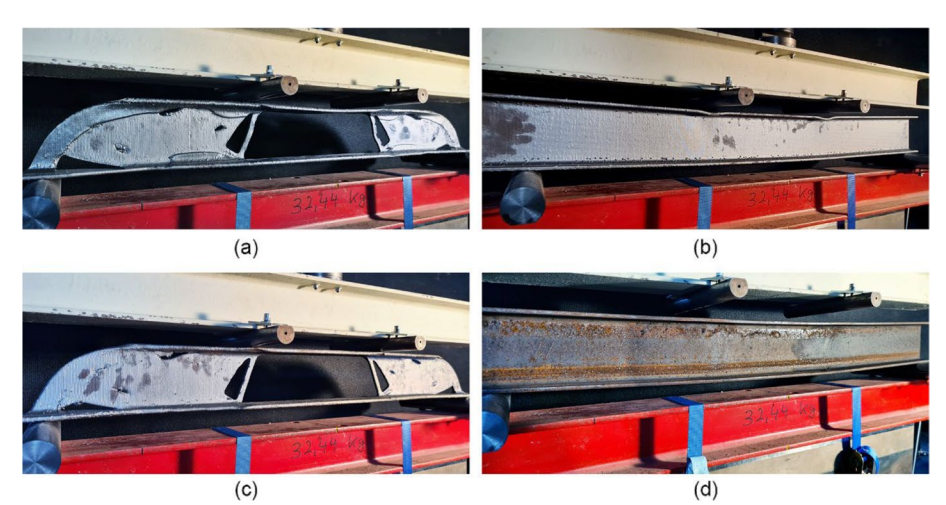


Fig. 17 Specimens B1-B4 testing (photos by Michael Herrmann/Technische Hochschule Luebeck)

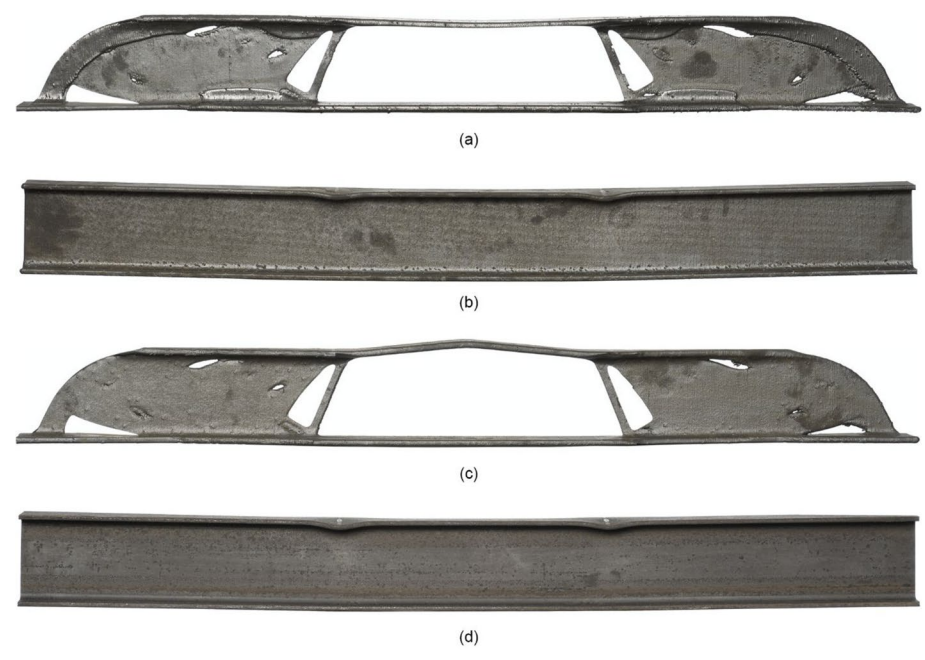


Fig. 18 The four structurally tested beams after loading with visible plastic deformations: (a) Specimen B1 (MMTO beam composed of mild steel and tool steel); (b) Specimen B2 (printed IPE-100 mild steel); (c) Specimen B3 (SMTO beam 100% mild steel); (d) Specimen B4 (rolled IPE-100 beam S235) (photos by Jann Aden/Technische Hochschule Luebeck)

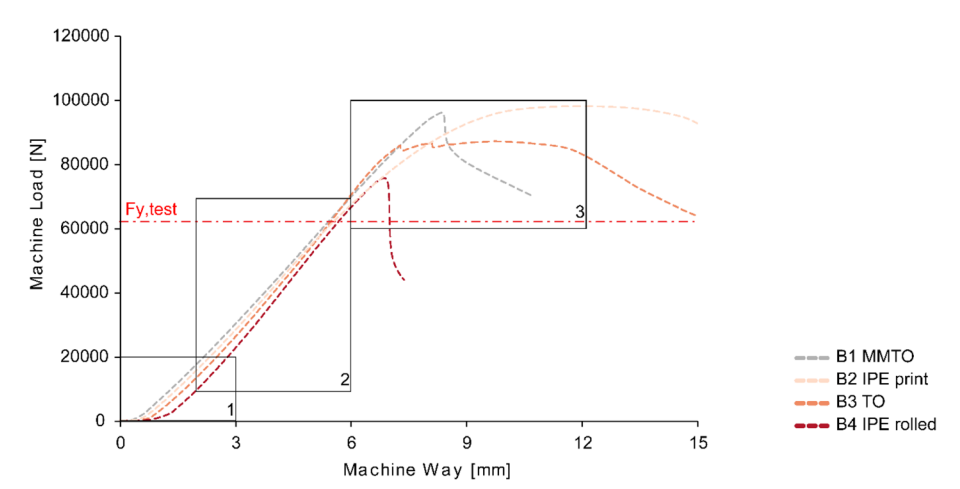


Fig. 19 Load displacement diagram of specimens B1-B4

observed failure mode of B4 is lateral torsional buckling of the upper flange. B1 reached its ultimate load at 96.3 kN and showed local buckling of the upper flange, with a first reduction in stiffness at approximately 85 kN. B2 reached the highest ultimate test load of all beams at 98.3 kN. It is also the first beam to show a decrease of stiffness at a load level of approximately 60 kN. Its failure mode was also lateral torsional buckling.

Figure 21 shows a side view of specimen B2 after unloading. The dotted line shows the assumed plastic deformation with plastic hinges formed in the beam

segment with constant bending moment between the two loading points. As previously stated, this failure pattern was also observed in specimen B4 and overlapped with lateral torsional buckling for both beams.

5.3 Comparison of results with standard IPE-100/ Discussion

Table 6 shows an overview of the test results. The optimisation goal was to minimise compliance, hence maximise the stiffness, while reducing mass. All four beams had a similar elastic bending stiffness with parallel

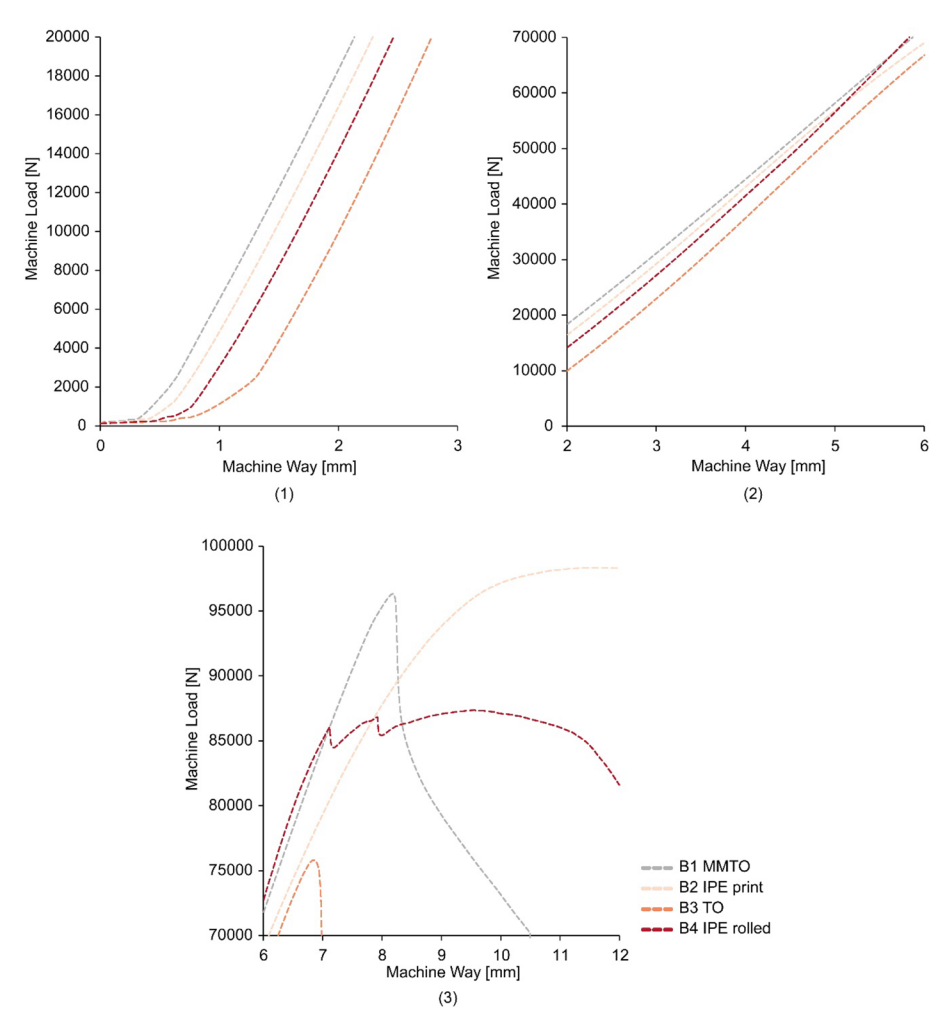


Fig. 20 Isolated area of interest of the load displacement diagram

increasing load deformation curves even though B1 and B3 are topologically optimised and have a reduced mass of 28% (B1) and 20% (B3) compared to the rolled IPE-100 beam B4. Therefore, it can be concluded that the optimisation objective function was fulfilled. All beams reached $F_{y,test,100,235} = 62kN$, which is the required test load for load bearing capacity. The faster declining graph after reaching $F_{ult, test}$ of the optimised beams can be explained by the local buckling of the upper flange. Additional webbing in the beam section of the constant bending moment would have led to a higher ultimate test load in the optimised beams. Comparing B1 to B3 it can

be stated that all structural performance parameters of the MMTO beam B1 exceeded those of the single material beam B3. A future question is whether $F_{\rm ult,\ test}$ of the full beams could have been increased by horizontally supporting the upper flange to prevent lateral torsional buckling, given that plastic moment hinges were also observed in those beams.

6 Conclusion

Regarding the structural load testing, the beam that reached its ultimate test load first was the mild steel (SMTO) beam, followed by the standard IPE-100. Both



Fig. 21 Specimen B2 showing plastic hinges under the loading points (photo by Jann Aden/Technische Hochschule Luebeck)

Table 6 Overview of the test results

| Test Name | Weight (g) | F _{y,test} (kN) | d _{y,test} (mm) | F _{ult,test} (kN) | d _{ult,test} (mm) | Weight/ Weight B4 (mm) |
|---------------------|---------------|-----------------------------|-----------------------------|-------------------------------|-------------------------------|------------------------------|
| B1 MMTO | 5,916 | 85.000 | 7.030 | 96.300 | 8.170 | 0.720 |
| B2 IPE (3D printed) | 7,770 | 60.000 | 5.250 | 98.300 | 11.330 | 0.940 |
| B3 SMTO | 6,583 | 70.000 | 6.250 | 75.700 | 6.800 | 0.800 |
| B4 IPE (rolled) | 8,226 | 80.000 | 6.510 | 86.000 | 7.110 | 1.000 |

the MMTO and the 3D printed mild steel equivalent of the standard beam achieved higher ultimate test loads than the standard IPE-100, with the MMTO beam demonstrating the best overall structural performance. Nonetheless, when considering the carbon emission benefits associated with reducing beam mass (excluding fabrication emissions), the MMTO beam is regarded as the better overall solution compared to both the full mass 3D printed beam and the standard IPE-100.

That said, previous research by two of the authors indicated the presence of residual stresses in a 3D printed metal bracket, which could compromise its performance (Grigoriadis et al., 2024). This may also be the case here, and further investigation is required to confirm it. It is worth noting that the beam rolling process inherently introduces residual stresses due to the high deformation and cooling rates during the multi-pass rolling process, which can potentially affect the final component behaviour. Regarding AM, as mentioned in Sect. 3.3, Meltio offers post-processing options commonly used in the industry-such as annealing and stress-relieving heat treatments—to address residual stresses. Furthermore, integrated thermal control and path planning algorithms, currently under development to mitigate residual stresses in LMD, could further enhance performance and reduce residual stress issues in MMTO metal beams and other building components.

Regarding the supports, a straightforward solution would be to recycle them. A key consideration in this process is the availability of a recycling facility near the fabrication site. If recycling the supports abroad—often the case for cost reasons—is necessary, the transport-related emissions must be included in the overall carbon footprint. Furthermore, if the energy used for melting the material predominantly comes from fossil fuels, the final carbon impact would increase substantially. Nonetheless, regardless of the recycling strategy, the use of supports inherently leads to longer printing times and higher embodied carbon from the outset.

Therefore, as discussed in Sect. 3.2, a next step in this research is to incorporate fabrication constraints—such as limiting angles to below 20–25 degrees from the printing axis—and/or to introduce additional

internal webbing within the optimisation process itself. While this approach removes the need for supports, it may lead to an increase in material usage compared with a TO process without constraints. Additionally, Meltio now offers advanced automatic support strategies that minimise, and in some cases eliminate, the need for supports by utilising multi-axis capabilities. Although Meltio systems can combine up to eight axes to improve robotic accessibility and avoid supports, the size and linearity of the part may limit this potential for certain geometries. Furthermore, as also discussed in Sect. 3.2, printing material in different orientations can cause variations in heating and cooling, leading to differential stresses and non-uniform structural performance. The application of these multi-axis capabilities to eliminate supports while maintaining predictable structural behaviour will also be explored further in the next phase of this research.

In terms of printing time, Gardner et al. (2020) and Shah et al. (2023) discuss the fabrication of a WAAM-²printed beam and a bridge in Amsterdam, respectively, reporting a typical deposition rate of 2 kg/h-approximately fourteen times higher than the rate used in this study. Shah et al. (2023) further note that increasing the deposition rate to 5 kg/h reduces the climate change impact of WAAM by 22%, and to 10 kg/h by 29%. However, WAAM has several inherent limitations: it offers lower dimensional precision, results in significantly rougher as-built surfaces, and the high heat input induces pronounced anisotropy in mechanical properties. Consequently, WAAM typically has lower deposition efficiency, leading to higher material wastage. Its lower resolution also necessitates the use of more material to achieve the required structural performance. Therefore, despite the higher deposition rates, the increased use of surplus material may offset the advantages of faster printing times. Any direct comparison of deposition rates should thus consider the final volume of 3D printed material required to achieve equivalent part strength. With

² Wire Arc Additive Manufacturing (WAAM) is an alternative metal 3D printing process to LMD.



Fig. 22 From top to bottom, MMTO beams with 20%, 30%, and 40% volume fraction

these considerations in mind, a subsequent phase of this research will focus on investigating significantly higher deposition rates³ which could substantially reduce printing time⁴ and, consequently, lower the associated carbon footprint.

The final two key parameters in the carbon emissions reduction process are the composition of the electricity grid and the degree of mass reduction achieved in the TO beam. Regarding the latter, Shah et al. (2023) note that, to achieve lower carbon emissions with WAAM compared to conventional hot rolling, a TO beam must have at least 50% less mass than a standard beam. In this study, the MMTO beam retained 50% of the full beam's mass but still had a higher carbon footprint—although, as previously mentioned, printing time is the main contributing factor. Consequently, MMTO beams with 40% mass or less will be investigated next (Fig. 22), including structural analyses to verify their performance. It should also be noted that an alternative method currently being explored by the authors involves local mass reduction using lattice geometries in structurally non-critical regions. For example, gyroid geometries-printable via LMD—could be incorporated into parts of the beam to introduce micro-perforations and reduce material use, thereby avoiding the need to re-optimise the beam for global mass reduction (Fig. 23).

Regarding the electricity mix, countries such as the UK currently rely on a combination of fossil fuels, renewables, and other sources, typically including nuclear and

biomass. As the UK moves towards its Net Zero target by 2050, the energy composition is expected to shift predominantly towards renewables, with nuclear and biomass comprising a smaller share. If biomass—considered more environmentally damaging than fossil fuels (Thunberg, 2022)—were excluded, the adoption of a 100% clean electricity grid could reduce the environmental impact of 3D printing by over 30% (Shah et al., 2023).

Effectively, summarising the future scenarios concerning embodied carbon reduction, as discussed in Sect. 3.4, using the current Meltio system could result in deposition rates up to 2.5 times higher. This would reduce the Total Electricity Consumption Emissions for 3D Printing (kgCO₂e) in Table 5 from 58.49 to 23.40. Additionally, assuming a 100% clean electricity supply, this figure would be reduced further to 16.40 kgCO₂e. Although this requires further investigation, if the relationship between beam mass and printing time were linear, and the beam printed belonged to the 20% volume fraction category (i.e. 2.5 times lighter than the one studied here), the total emissions would be reduced to 6.56 kgCO₂e (assuming no supports were required for printing). In the case of a 20% mass, the Total Material+Filament Production Emissions (kgCO₂e) would also be 2.5 times lower, at 4.96. In principle, therefore, the combined total would be 6.56 + 4.96 = 11.52 (kgCO₂e), which is 40% lower than that of the conventional IPE 100.

Finally, while the design and optimisation methods outlined above are well-established and technically robust, the optimisation process used is not specifically tailored for architects seeking to integrate structural and aesthetic considerations—particularly in research such as this, which also explores the architectural potential of MMTO components. For this reason, it would be worthwhile to investigate the design and optimisation of the MMTO beam using the newly released Grasshopper plugin *Stag*

 $^{^{\}overline{3}}$ Comparing the deposition rates of each method to the total volume of printed material will allow for the identification of the more energy-efficient and sustainable of the two.

⁴ At the time of writing, Meltio's current blue laser system can achieve deposition rates exceeding 0.6 kg/h for certain alloys. Additionally, a higher-powered laser, currently under development and expected for release next year, promises even faster printing speeds.

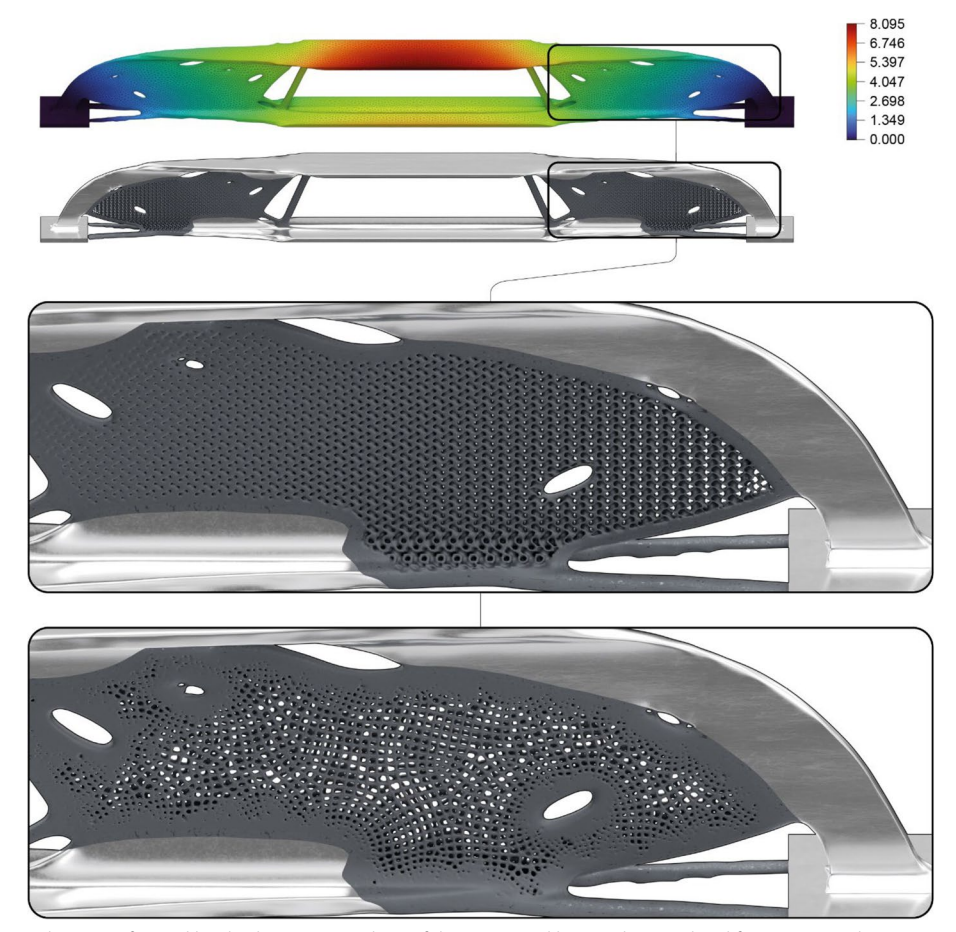


Fig. 23 Local mass reduction informed by displacement analysis of the optimised beam. The top detail features gyroid geometries with varying densities corresponding to displacement levels—regions experiencing lower displacement contain larger gyroids. The bottom detail employs a square honeycomb lattice, which may not be feasible to print using LMD

(Damtsas et al., 2025), which is specifically developed with architects in mind. Since Grasshopper is native to Rhinoceros3D, the use of Stag would retain the same design starting point while offering a more intuitive and designer-friendly workflow.

Furthermore, Stag's optimisation algorithm uses the SIMP method, making it directly comparable to the process employed in this research. As demonstrated by

Damtsas et al. (2025), Stag's results are topologically similar to those obtained from established methods found in the literature, commercial software, and other TO plugins for Grasshopper. In terms of capabilities, Stag can perform MMTO with more than two materials within design domains that are both regular and irregular, including multiple passive solid and void areas (Damtsas et al., 2024, 2025). An example with a similar setup to the

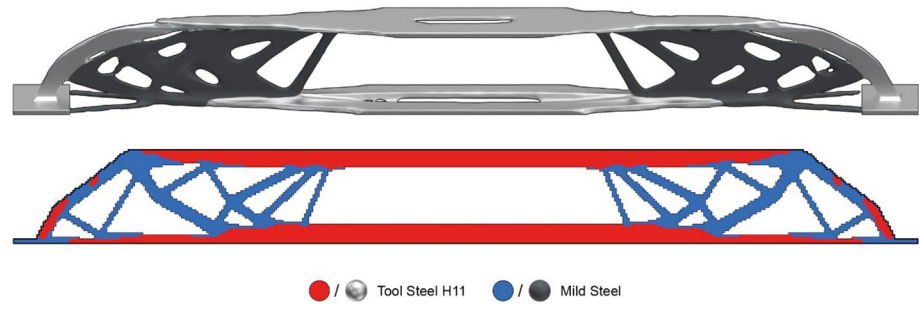


Fig. 24 MMTO Beam (40% volume fraction: 40% mild steel, 60% tool steel) optimised using Altair (top) and Stag (bottom)

one used in this research can be seen in Fig. 24, where Altair's Optistruct result is compared to Stag's. However, the design and optimisation were performed as a 2D shell, as Stag is currently only available in 2D. If it were to be used in place of Altair's software for this research, its development to support 3D MMTO would be required.

To conclude, applying TO to the AM of building components warrants further development, particularly in reducing printing times, manufacturing constraints, and costs. Scaling MMTO beams to full construction lengths is currently constrained by the reach of the robotic arm, as vertical printing is required to prevent collisions and maintain consistent layer orientation. The maximum vertical 3D print length currently achievable is 6.2 m (FANUC America Corporation, 2025), whereas hotrolled I-beams typically range from 4 to 12 m (Metinvest, 2006), and up to 18 m (Delta Steel, 2025). Although horizontal track-based 3D printing enables lengths beyond robotic vertical reach, MMTO beams cannot be produced in this orientation without multiple toolpath adjustments (Fig. 10), which introduce anisotropy into their structural behaviour.

Effectively, as this and related studies demonstrate, further progress is required in the design, testing, and validation of multi-metal building components. Nonetheless, research in this area is advancing rapidly and is expected to proliferate in the near future.

Acknowledgements

This research was conducted collaboratively between University College London, the University of Applied Sciences Luebeck, and industry partners Foster + Partners and Meltio. Special thanks go to Altair Engineering Ltd for providing the educational license used in this project and to Gerardo Xavier Zurita Campaña and Jairo Luengo Fernandez for their contributions to the project as part of the Meltio team.

Authors' contributions

All authors contributed to the study and discussed the results. Specifically, E.D: Writing – Abstract; Sect. 1 (part); Sect. 2; Sect. 6 (part); Review and editing of the article, tables and figures. A.N.J: Writing—Sect. 3; M.K: Review of the article; M.H: Writing—Sect. 6; K.G: Principal investigator of the research; Research supervision; Research project management; funding acquisition; Writing—Sects. 1 (part); 4; 6 (part); and review and editing of the article, tables and figures.

Funding

This work was supported by the Bartlett Innovation Fund of The Bartlett Faculty of the Built Environment at University College London.

Data availability

The data supporting the findings of this study are available from the authors upon reasonable request.

Declarations

Ethics and Consent to Participate

Not applicable as no research involving humans and/or animals was undertaken.

Consent to Publication

All authors consent to the publication of this research.

Competing interests

The authors declare that no competing financial interests exist. Kostas Grigoriadis is a member of the Editorial Board (Associate Editor) for Architectural Intelligence but was not involved in the reviews or any decisions related to this submission.

Received: 16 July 2025 Revised: 10 September 2025 Accepted: 29 September 2025

Published online: 24 November 2025

References

- Albert, A. H. (2024). Schneider Bautabellen für Ingenieure (26th ed.). Reguvis Fachmedien.
- Altair Engineering Inc. (2021a). *Design Elements*. Retrieved May 8, 2023, from https://2021.help.altair.com/2021/hwsolvers/os/topics/solvers/os/topology_opt_design_elements_r.htm
- Altair Engineering Inc. (2021b). *Tetra Meshing*. Retrieved May 5, 2025, from https://2021.help.altair.com/2021/hwdesktop/hm/topics/pre_processing/meshing/meshing_tetra_c.htm
- Altair Engineering Inc. (2022a). Optimization Responses. Retrieved August 1, 2025, from https://2022.help.altair.com/2022.1/hwdesktop/hwx/topics/pre_processing/entities/optimization_responses_r.htm
- Altair Engineering Inc. (2022b). *Responses*. Retrieved August 1, 2025, from https://2022.help.altair.com/2022.1/hwsolvers/os/topics/solvers/os/responses.htm
- Altair Engineering Inc. (2024). *Design Variables*. Retrieved January 6, 2025, from https://2024.help.altair.com/2024/hwsolvers/os/topics/solvers/os/topology opt design variables r.htm
- Altair Engineering Inc. (2025a). *Design Elements*. Retrieved February 25, 2025, from https://help.altair.com/hwsolvers/os/topics/solvers/os/topology_opt_design_elements_r.htm
- Altair Engineering Inc. (2025b). DOPTPRM, MINDIM. Retrieved February 25, 2025, from https://help.altair.com/hwsolvers/os/topics/solvers/os/doptprm_mindim_bulk_r.htm
- Amir, O., & Mass, Y. (2018). Topology optimization for staged construction. Structural and Multidisciplinary Optimization, 57, 1679–1694.
- Chiu, L. N., Rolfe, B., Wu, X., & Yan, W. (2018). Effect of stiffness anisotropy on topology optimisation of additively manufactured structures. *Engineering Structures*, 171, 842–848.
- Damtsas, E., Banh, T., Lee, D., & Herrmann, M. (2024). Two-way connection between Grasshopper and Matlab for the first SIMP-based multi-material topology optimisation plugin for Grasshopper. In *eCAADe Proceedings*, 2, 375–382. https://doi.org/10.52842/conf.ecaade.2024.2.375
- Damtsas, E., Banh, T.T., Lee, D., & Herrmann, M. (2025). A closed loop methodology for two-dimensional multi-material topology optimization in Grasshopper using the generalized SIMP method. *Architectural Science Review*, 1–15. https://doi.org/10.1080/00038628.2025.2476640
- Esfarjani, S. M., Dadashi, A., & Azadi, M. (2022). Topology optimization of additive-manufactured metamaterial structures: A review focused on multi-material types. *Forces in Mechanics*, 7, Article 100100.
- EurocodeApplied. (2025). *Table of properties for IPE,HEA,HEB,HEM,UB,UC,UBP profiles Eurocode 3*. Retrieved March 3, 2025, from https://eurocodeapplied.com/design/en1993/ipe-hea-heb-hem-design-properties
- FANUC America Corporation. (2025). FANUC M-2000 series robots Ultra heavy payload robots up to 2300 kg. Retrieved September 4, 2025, from https://www.fanucamerica.com/products/robots/series/m-2000
- Gardner, L., Kyvelou, P., Herbert, G., & Buchanan, C. (2020). Testing and initial verification of the world's first metal 3D printed bridge. *Journal of Con*structional Steel Research, 172, Article 106233. https://doi.org/10.1016/j. icsr.2020.106233
- Grigoriadis, K., Bouchard, J., & Herrmann, M. (2024). Topologically optimised facade brackets: An embodied carbon, structural and residual stress analysis. *Architectural Intelligence*, *3*(1), 22. https://doi.org/10.1007/s44223-024-00063-2
- Grigoriadis, K., & Lee, G. (2024). 3D printing and material extrusion in architecture: Construction and design manual. DOM publishers.

- Habashneh, M., & Rad, M. M. (2024). Plastic-limit probabilistic structural topology optimization of steel beams. *Applied Mathematical Modelling*, 128, 347–369
- Hashimoto, T., Terasaki, H., & Komizo, Y.-l. (2009). Solidification cracking susceptibility of alloy tool steel under rapid solidification. *Quarterly Journal of the Japan Welding Society, 27*(2), 126s–129s.
- Hoglund, R., & Fuerle, F. (2018). Design Optimization for Additive Manufacturing in OptiStruct with consideration of Overhang Angle in Topology Optimization. Altair Engineering Inc. Retrieved September 1, 2025, from https://altair.com/docs/default-source/resource-library/design-optimization-foram-in-optistruct-with-consideration-of-oha-in-topology-optimization.pdf?sfvrsn=f951db3d 3
- Hoglund, R. (2024). Create a DRESP2 using a function for OptiStruct optimization in HyperWorks. Altair Engineering Inc. Retrieved August 4, 2025, from https://community.altair.com/discussion/39519/create-a-dresp2-using-a-function-for-optistruct-optimization-in-hyperworks/p1
- Jayasankar, D. C., Gnaase, S., Kaiser, M. A., Lehnert, D., & Tröster, T. (2024).
 Advancements in hybrid additive manufacturing: Integrating SLM and LMD for high-performance applications. *Metals*, 14(7), Article 772.
- Kingman, J., Tsavdaridis, K. D., & Toropov, V. V. (2014). Applications of topology optimization in structural engineering. In *Civil engineering for sustainability* and resilience international conference (CESARE).
- Lagaros, N. D., Psarras, L. D., Papadrakakis, M., & Panagiotou, G. (2008). Optimum design of steel structures with web openings. *Engineering Structures*, 30(9), 2528–2537. https://doi.org/10.1016/j.engstruct.2008.02.002
- Laghi, V., Palermo, M., Bruggi, M., Gasparini, G., & Trombetti, T. (2022). Blended structural optimization for wire-and-arc additively manufactured beams. *Progress in Additive Manufacturing, 8*(3), 381–392. https://doi.org/10.1007/s40964-022-00335-1
- Li, Y., & Xie, Y. M. (2021). Evolutionary topology optimization for structures made of multiple materials with different properties in tension and compression. *Composite Structures*, 259, Article 113497.
- Meltio3D. (2025). Meltio Materials Metal AM Wires. Meltio3D. Retrieved February 25, 2025, from https://meltio3d.com/materials/
- MetalTek International. (2024). Alloy Steel vs. Carbon Steel: Your Complete Guide-MetalTek. Retrieved September 1, 2025, from https://www.metaltek.com/blog/alloy-steel-vs-carbon-steel-your-complete-guide/
- Metinvest. (2006). *I-beams*. Retrieved September 4, 2025, from https://metinvestholding.com/en/products/long-products/i-beams
- Persson, A., Hogmark, S., & Bergström, J. (2005). Thermal fatigue cracking of surface engineered hot work tool steels. Surface and Coatings Technology, 191(2–3), 216–227.
- Ribeiro, T. P., Bernardo, L. F., & Andrade, J. M. (2021). Topology optimisation in structural steel design for additive manufacturing. *Applied Sciences*, 11(5), 2112
- Robbins, J., Owen, S., Clark, B., & Voth, T. (2016). An efficient and scalable approach for generating topologically optimized cellular structures for additive manufacturing. *Additive Manufacturing*, *12*, 296–304. https://doi.org/10.1016/j.addma.2016.06.013
- Saufnay, L., Jaspart, J. P., & Demonceau, J. F. (2021). Economic benefit of high strength steel sections for steel structures. Ce/papers, 4(2–4), 1543–1550. https://doi.org/10.1002/cepa.1454
- Shah, I. H., Hadjipantelis, N., Walter, L., Myers, R. J., & Gardner, L. (2023). Environmental life cycle assessment of wire arc additively manufactured steel structural components. *Journal of Cleaner Production*, 389, Article 136071.
- Stahlwerk Thuringen GmbH. (2025). How our steel is produced: The section rolling mill. Retrieved March 3, 2025, from https://www.stahlwerk-thueringen.com/company/production_process/productionprocess?loopID= 14893365CD8
- Delta Steel. (2025). *I-beams Delta Steel*. Retrieved September 4, 2025, from https://www.deltasteel.com/products/i-beams/
- Thunberg, G. (2022). The Climate Book (1st ed.). Penguin Books Ltd.
 Tsavdaridis, K. D., Kingman, J. J., & Toropov, V. V. (2015). Application of structural topology optimisation to perforated steel beams. Computers and StructurEs, 158, 108–123.
- Tsavdaridis, K. D., Kingman, J., & Toropov, V. (2014). Structural topology optimisation in steel structural applications. In *Proceedings of the Hellenic National Conference of Steel Structures*.
- Wethyavivorn, B., Surit, S., Thanadirek, T., & Wethyavivorn, P. (2022). Topology optimization-based reinforced concrete beams: Design and experiment. *Journal of Structural Engineering*, 148(10), 04022154.

- Ye, J., Kyvelou, P., Gilardi, F., Lu, H., Gilbert, M., & Gardner, L. (2021). An endto-end framework for the additive manufacture of optimized tubular structures. *IEEE Access*, *9*, 165476–165489.
- Zhai, W., Guo, Y., Canturri, C., Shandro, R., & Zhou, W. (2024). Wire arc additive manufacturing of ER70S-6/S355 bimetal component. *Materials Science and Engineering A, 900*, Article 146498.

Publisher's Note

Springer Nature remains neutral with regard to jurisdictional claims in published maps and institutional affiliations.